



Investigation of structural, optical, and dielectric properties of $\text{Zn}_{1-x}\text{Cr}_x\text{S}$ nanoparticles for optoelectronic applications

V. V. Jadhavar^{1,*}  and B. S. Munde^{2,*}

¹Thin Films and Materials Science Research Laboratory, Department of Physics, Dayanand Science College, Latur, Maharashtra 413512, India

²Department of Physics, K.K.M. College, Manwath, Maharashtra, India

Received: 28 June 2022

Accepted: 13 September 2022

Published online:
24 September 2022

© The Author(s), under exclusive licence to Springer Science+Business Media, LLC, part of Springer Nature 2022

ABSTRACT

We investigated the structure, optical, and dielectric properties of undoped and chromium-doped zinc sulfide ($\text{Zn}_{1-x}\text{Cr}_x\text{S}$) nanoparticles prepared via co-precipitation at 300 K with Cr concentrations $x = 0.00, 0.02,$ and 0.04 . The X-ray diffraction patterns demonstrated that the $\text{Zn}_{1-x}\text{Cr}_x\text{S}$ nanoparticles have a cubic structure with no impurity. The average crystallite size of the nanoparticles calculated using the Scherrer equation is in the range of 1.70–1.56 nm and decreases with an increase in Cr content. The lattice constants were in the range of 5.38–5.35 Å. Field emission scanning electron microscope (FESEM) images of nanoparticles show nearly spherical morphology with agglomeration, and doping reduces agglomeration. Energy-dispersive spectroscopy (EDS) analysis confirmed the presence of Cr in doped samples. The optical band gap of undoped ZnS nanoparticles was found to be 3.35 eV, increasing slightly from 3.39 to 3.41 eV as the chromium concentration increased. Dielectric measurements show that the dielectric constant of doped samples is higher at low frequencies, whereas the dielectric losses of these samples are lower at higher frequencies. Furthermore, the AC conductivity of all samples varies with frequency and composition, increasing abruptly at higher frequencies and decreasing with the addition of Cr ion in the ZnS matrix. Optical and dielectric results indicate that Cr-doped ZnS nanoparticles are promising materials for optoelectronic and high-frequency devices.

Address correspondence to E-mail: jadhavarvikas@gmail.com; bhaskarsmunde@gmail.com

1 Introduction

Recent research on nanoscale materials has revealed great opportunities for a wide range of technological applications [1, 2]. Nanoparticle semiconductors differ from bulk semiconductors. Semiconductor nanoparticles have distinct physical, chemical, optical, electrical, and magnetic properties compared to bulk because of their nano size and large surface area-to-volume ratio, which makes them potentially useful in a wide range of technological fields, including optoelectronics, spintronics, field emitters, displays, sensors, lasers, etc. [3–6]. Zinc sulfide (ZnS), a technologically important II-VI compound semiconductor, has been extensively studied due to its broad band gap energy of 3.68 eV at room temperature [7–9]. It has two different types of crystal structures: cubic and hexagonal. ZnS is a non-toxic and low-cost element that is readily available in nature. ZnS is the most chemically stable II-VI semiconductor owing to its excellent physical, electrical, and optical properties caused by the quantum confinement effect [10]. ZnS nanoparticles have a wide range of applications, including solar cells, gas sensors, flat panel displays, cathode ray tubes, LEDs, photovoltaics, photoconductors, optical fibers, optical sensors, phosphors, infrared windows, etc. [11–18]. The properties of ZnS nanoparticles can be modified by doping with foreign elements to achieve the above-mentioned applications.

Transition metal ions play a significant role in improving the optical, electrical, and magnetic properties of ZnS nanoparticles at room temperature. Cr dopant is one of the more interesting dopant elements and has received a lot of attention [19, 20]. Cr was chosen as a dopant because it has unique abundant electron shell structure and has a smaller ionic radius (0.63 Å) than Zn^{2+} (0.74 Å), allowing Cr^{3+} to easily penetrate the ZnS crystal lattice [21]. Furthermore, during the substitution of ZnS, Cr becomes Cr^{3+} , implying one more electron that contributes to electrical conduction. The incorporation of Cr into ZnS nanoparticles has received a lot of attention due to their interesting optical and dielectric properties. Cr-doped ZnS is attractive for a variety of optoelectronic [22] and spintronic applications [8], as well as solar cells [23]. Several research groups have studied the effect of Cr doping on ZnS nanoparticles. AL-Osta et al. [24] investigated the optical properties of Cr-doped ZnS nanoparticles using the chemical co-

precipitation method and found that the optical band gap energy increased with Cr doping due to the blue shift in the absorption edge. Samba Vall et al. [25] reported that the band gap of Cr-doped ZnS thin films decreases with increasing Cr concentration due to a decrease in the number of grain boundaries caused by the increasing crystallite size of thin films. According to Reddy et al. [26], the increase in band gap of Cr-doped ZnS nanoparticles with increasing Cr concentration is due to the size quantization effect caused by the small particle size, whereas Prabhu et al. [27] observed a decrease in band gap of Cr-ZnS nanoparticles due to particle size reduction caused by the quantum confinement effect within nanoparticles. Aqeel et al. [28] revealed that the increase in band gap energies of Cr-doped ZnS nanoparticles with the Cr addition is due to a decrease in crystallite size caused by doping. Besides this, Virpal et al. [29] discovered a significant increase in dielectric constant in chromium-doped zinc sulfide nanoparticles caused by the combined effect of the Maxwell–Wagner phenomenon and microscopic spontaneous polarization. Osman Gurbuz et al. [30] prepared Cr-doped ZnO thin films at room temperature using a magnetron sputtering technique and found that electrical conductivity increases while dielectric constant decreases with Cr content. According to Selmi et al. [31], doping ZnO with Cu at a low concentration results in a high dielectric constant and a low tangent loss. They also discovered an increase in AC conductivity as Cu content increased. Khan et al. [32] noticed a significant decrease in the dielectric constant and loss due to Ni incorporation into the ZnO lattice. Also, they observed a sudden increase in AC conductivity at high frequencies. Nevertheless, there has been little research on the dielectric properties of ZnS nanoparticles doped with chromium at low concentrations, so more research is needed. As a result, we used low concentrations of chromium to dope the ZnS material. For the preparation of ZnS nanoparticles, several physical and chemical methods have recently been reported, such as ball milling [33], sputtering [34], co-evaporation [35], sol–gel [36], co-precipitation [37], hydrothermal [38], etc. We chose co-precipitation over the other methods because of its ease of use, low equipment costs, lower processing temperatures, and environmental friendliness. This method is superior to others because the reagents are mixed at the molecular level. As a result,

stoichiometry, morphology, purity, and homogeneity are all well maintained.

In the present investigation, we have successfully prepared Cr-doped ZnS nanoparticles using the co-precipitation method at room temperature. Moreover, the structural, morphological, optical, and dielectric properties of the Cr-doped ZnS nanoparticles are systematically characterized to study the crystal structure, morphology, optical, and dielectric behavior. Cr was found to be important in promoting the structural, optical, and dielectric properties of ZnS nanoparticles.

2 Experimental

2.1 Materials

Undoped ZnS and Cr-doped ZnS nanoparticles were synthesized using analytical grade zinc acetate dehydrate [$\text{Zn}(\text{CH}_3\text{COO})_2 \cdot 2\text{H}_2\text{O}$], sodium sulfide [$\text{Na}_2\text{S} \cdot \text{H}_2\text{O}$], and chromium nitrate [$\text{Cr}(\text{NO}_3)_3 \cdot 9\text{H}_2\text{O}$] as zinc, sulfur, and chromium sources, respectively. Sample preparation was done with double distilled water as a solvent. The ethanol is used for washing purposes. These chemicals have been purchased from Merk.

2.2 Preparation of $\text{Zn}_{1-x}\text{Cr}_x\text{S}$ nanoparticles

The flow chart for the preparation of $\text{Zn}_{1-x}\text{Cr}_x\text{S}$ nanoparticles using the co-precipitation method at room temperature is shown in Fig. 1.

The synthesis procedure is as follows: To make a 1 M solution, the desired amounts of zinc acetate dehydrates, chromium nitrate, and sodium sulfide were dissolved separately in three beakers, each containing 100 ml of double distilled water. For 1 h, these solutions are continuously stirred with a magnetic stirrer to achieve complete dissolution. Following that, a 1 M chromium nitrate solution was added to the 1 M zinc acetate solution, which was kept stirring. Add 1 M sodium sulfide drop-wise to the above stirred solution with continuous vigorous stirring. After 2 h of uniform stirring, a fine precipitate was formed. For sodium impurity extraction, a precipitate containing Cr-doped ZnS nanoparticles was filtered using Whatman paper. The wet precipitate is washed with double distilled water several times, and the remaining water is rinsed out with a

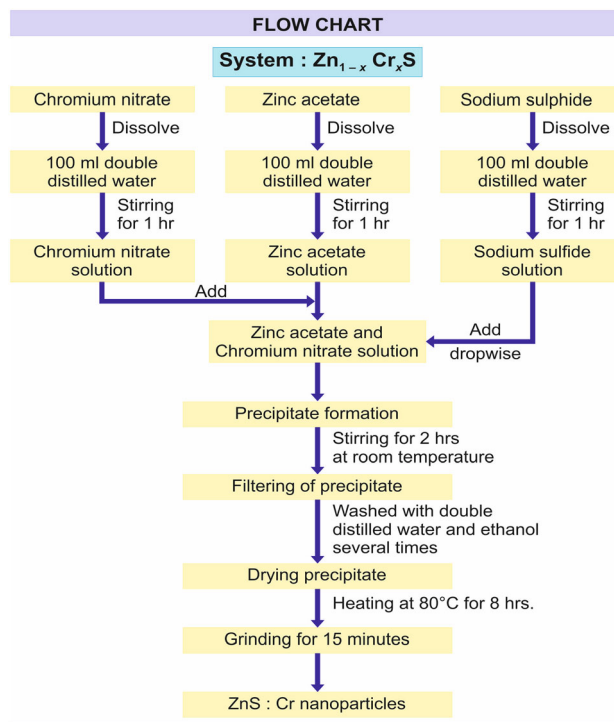


Fig. 1 Flowchart for preparation of $\text{Zn}_{1-x}\text{Cr}_x\text{S}$ nanoparticles

few washes of ethanol. The prepared samples were dried at room temperature before being placed in an oven at 80 °C for 8 h to remove the water content. The dried samples were finally crushed into a fine powder using a mortar and pestle.

The prepared $\text{Zn}_{1-x}\text{Cr}_x\text{S}$ nanoparticles are then used to investigate their structural, morphological, compositional, optical, and dielectric properties. Moreover, to study the dielectric properties, a certain amount of powder was used for the preparation of pellets. The opposite faces of pellets were then coated with silver paste to make ohmic contact.

2.3 Characterization techniques

The $\text{Zn}_{1-x}\text{Cr}_x\text{S}$ nanoparticles were characterized using a variety of experimental techniques. The structural characteristics were investigated using a Rigaku Ultima IV X-ray diffractometer with a monochromatic Cu-K_α radiation source of wavelength 1.54056 Å. XRD data were taken in the range of 20–80 °C at room temperature. A field emission scanning electron microscope (FE-SEM) linked to an energy-dispersive x-ray analyzer (EDS) was used to study the surface morphology and chemical analysis of the prepared samples, respectively (CARL ZEISS

Sigma IV). The optical absorption spectra of prepared nanoparticles in the wavelength range of 200–800 nm were obtained using a UV–visible spectrometer (JASCO V-730) to calculate the energy band gap. Dielectric properties were investigated at 300 K using an LCR Meter (Hioki 3532-50 LCR Hi Tester) in the 5 Hz to 50 MHz frequency range.

3 Results and discussion

3.1 Structural studies

XRD patterns for $\text{Zn}_{1-x}\text{Cr}_x\text{S}$ nanoparticles with Cr concentrations of $x = 0.00, 0.02,$ and 0.04 are shown in Fig. 2. For each sample, the patterns show three well-formed diffraction peaks. These peaks are found at 2θ values of $28.63^\circ, 47.96^\circ,$ and 56.22° , which correspond to the (111), (220), and (311) reflection planes of cubic ZnS, respectively. All of the peaks are well matched to the standard diffraction patterns (JCPDS card number 03-0570). This confirmed that the crystal structure of the prepared nanoparticles is cubic. In the XRD patterns, the impurity peaks related to chromium clusters or chromium oxides were not seen, showing the single-phase sample formation, which indicates that the dopant Cr has entered the ZnS lattice sites. Poornaprakash et al. [39] and Kaur et al. [40] observed similar single-phase cubic structure of nanoparticles in their XRD patterns of $\text{Zn}_{1-x}\text{Cr}_x\text{S}$ nanoparticles. Furthermore, all of the samples

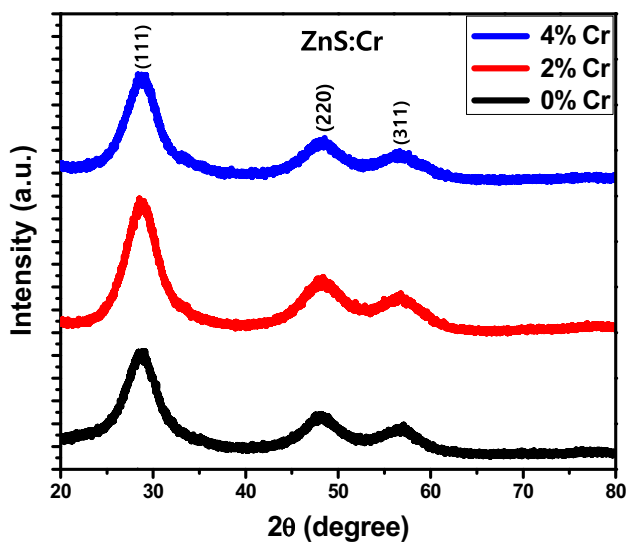


Fig. 2 X-ray diffraction patterns of $\text{Zn}_{1-x}\text{Cr}_x\text{S}$ nanoparticles

exhibited broad XRD peaks, indicating the presence of nanostructured particles.

The lattice constant of $\text{Zn}_{1-x}\text{Cr}_x\text{S}$ nanoparticles was determined using the formula [25]

$$a = \frac{\lambda}{2 \sin \theta} \sqrt{h^2 + k^2 + l^2}, \quad (1)$$

where λ denotes the wavelength of Cu- K_α radiation, θ denotes Bragg's angle, and (h, k, l) the miller indices of plane. As the Cr concentration increases, the lattice constant decreases from 5.38 to 5.35 Å (Table 1), indicating that Cr^{2+} ions replace Zn^{2+} ions in the ZnS lattice [8, 41]. Besides that, as the Cr content increases, the cell volume of doped samples decreases in comparison to undoped ZnS, indicating that Cr atoms are successfully doped. The average crystallite size (D) of $\text{Zn}_{1-x}\text{Cr}_x\text{S}$ nanoparticles was estimated using the Debye–Scherrer formula [12]

$$D = \frac{K\lambda}{\beta \cos \theta}, \quad (2)$$

where K is the particle shape factor (0.9), λ is the wavelength of X-rays used, β is the full-width half maxima of the diffraction peak, and θ is the angle of diffraction. As the Cr content increases, the average crystallite size of the nanoparticles decreases (shown in Table 1). This is due to the replacement of Zn^{2+} ions by Cr^{3+} ions during the formation of Cr-doped ZnS nanoparticles. Further, the microstrain (ε) of ZnS nanoparticles is calculated using the Stokes–Wilson equation [42]

$$\varepsilon = \frac{\beta \cos \theta}{4} \quad (3)$$

The microstrain is observed to increase from 23.05×10^{-2} to 24.92×10^{-2} with an increasing Cr doping concentration, as shown in Table 1. It may be due to a decrease in crystallite size. Furthermore, the dislocation density (δ), which represents the amount of defects in the prepared nanoparticles, is defined as the length of dislocation lines per unit volume of the crystal and is calculated using the Williamson and Smallman equation [43]

$$\delta = \frac{1}{D^2}, \quad (4)$$

where D is the average crystallite size (nm). The dislocation density is found to increase with increasing Cr content and is listed in Table 1. This demonstrates that as the size of the crystallites decreased, the matrix defects increased, implying

Table 1 Structural parameters of Zn_{1-x}Cr_xS nanoparticles

Dopant concentration	Lattice constant (Å)	Cell volume (Å) ³	Crystallite size (nm)	Micro strain $\varepsilon \times 10^{-2}$	Dislocation density $\delta \times 10^{-2}$ (lines/m ²)
0.00	5.3814	155.86	1.7043	23.05	35.17
0.02	5.3684	154.75	1.6445	23.68	38.76
0.04	5.3575	153.81	1.5601	24.92	44.47

that the crystallinity of Cr-doped ZnS nanoparticles decreased.

3.2 Morphological studies

FESEM is an extremely useful instrument for investigating the surface morphology of nanoparticles. The surface morphologies of undoped and Cr-doped ZnS nanoparticles are shown in Fig. 3. The images clearly show that the morphologies of doped samples differ from those of undoped samples. Undoped ZnS only shows clouds of agglomerations, whereas Cr-doped ZnS clearly shows agglomerated particles. The agglomeration among the particles is observed to decrease with an increase in Cr concentration. In addition, some of the agglomerated particles in doped samples appear to be nearly spherical. Reddy et al. [26] also discovered a decrease in agglomeration with an increase in Cr concentration while studying the morphological properties of Cr-doped ZnS nanoparticles.

3.3 Compositional studies

The EDS spectra of Zn_{1-x}Cr_xS nanoparticles are shown in Fig. 4. Figure 4a depicts the spectrum of an undoped ZnS sample, revealing the presence of Zn and S elements, whereas Fig. 4b–c depicts the spectra of Cr-doped samples, revealing the presence of Cr, Zn, and S elements. This clearly demonstrates that the prepared samples do not contain any foreign elements, as confirmed by XRD studies. This implies that all the samples are pure. Table 2 shows the chemical composition of Cr-doped ZnS nanoparticles. The amount of Cr found in 2% and 4% Cr-doped samples is 0.82% and 1.15%, respectively. The amount of Cr observed is less than that of the actual doped Cr because unreacted Cr atoms were removed during the washing process. The EDS spectra study also confirmed that the percentage of atomic weight

of Cr increased with increasing Cr content. This means the Cr³⁺ ions were successfully incorporated into the ZnS host matrix.

3.4 Optical studies

Optical properties are important in determining the band gap of semiconductor nanoparticles. Here, the band gap of the nanoparticles was estimated using the UV–vis absorption spectrum. The technique works on the principle that incident photons cause electronic transitions between the valence and conduction bands. The absorption of photons between different energy bands determines the band gap energy (E_g). The UV–vis absorption spectra of Zn_{1-x}Cr_xS nanoparticles at room temperature are shown in Fig. 5. The absorption edge for an undoped ZnS sample is 344 nm. The maximum absorption (λ_{ab}) for doped samples with $x = 0.02$ and 0.04 is observed at 343 and 342 nm, respectively. This indicates that the absorption edges of doped samples were slightly shifted toward shorter wavelengths when compared to undoped ZnS. As a result, a blue shift in the absorption edge has been observed for doped samples as the Cr concentration increases. Thus, the UV–vis spectra study not only confirms the decrease in crystallite size observed in XRD studies, but also suggests that increasing the Cr concentration in ZnS nanoparticles increases the energy band gap.

Tauc's plot, which describes the optical properties of amorphous materials, can be used to determine the optical band gap in semiconductors. Tauc proposed a relationship between the absorption coefficient (α) and the incident photon energy ($h\nu$) as [27]

$$\alpha h\nu = B(h\nu - E_g)^n, \quad (5)$$

where α is the absorption coefficient, B is a constant, h is Planck's constant, ν is the photon frequency, and E_g is the energy band gap. Depending on the type of

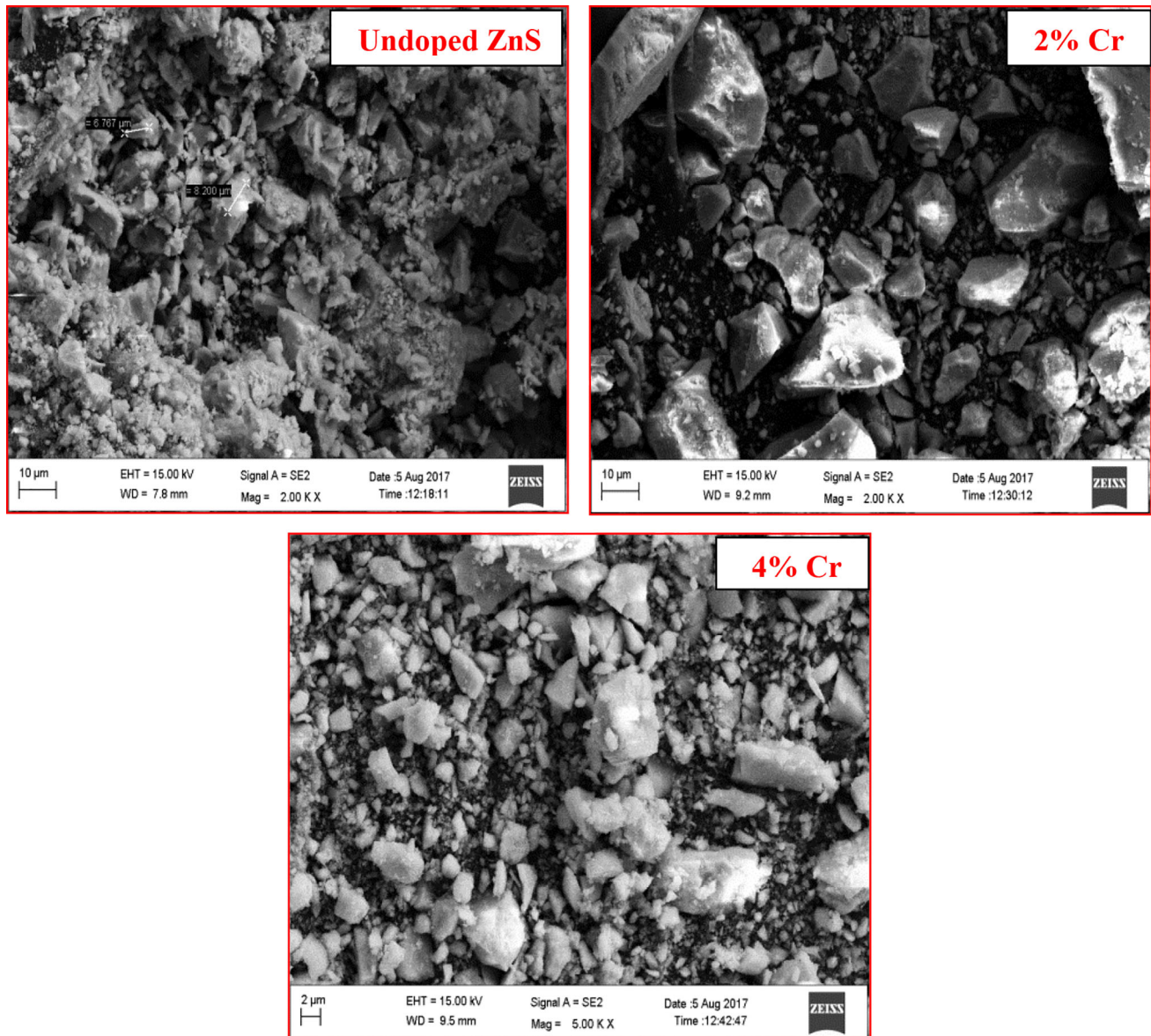


Fig. 3 FE-SEM images of $Zn_{1-x}Cr_xS$ nanoparticles

transition, exponent “ n ” can have values of $1/2$, 2 , $3/2$, and 3 , which correspond to the allowed direct, allowed indirect, forbidden direct, and forbidden indirect transitions, respectively [44]. Since ZnS has a direct band gap semiconductor, the value of n will be $1/2$. The energy band gap is determined by plotting the graph of $(\alpha h\nu)^2$ versus $h\nu$. Figure 6 shows Tauc’s plot of $Zn_{1-x}Cr_xS$ nanoparticles. The presence of a linear part in this graph provides additional evidence that ZnS is a direct band gap material. The linear fitting of the straight portion of the curve on the $h\nu$ axis gives the value of E_g . Tauc’s plot shows that the band gap energy for samples with $x = 0.00$, 0.02 , and

0.04 is 3.35 , 3.39 , and 3.41 eV, respectively, and that it increases as Cr content increases. These findings are similar to those reported by Reddy et al. [26]. In the present investigation, the optical band gap of $Zn_{1-x}Cr_xS$ nanoparticles increases with a reduction in crystallite size due to electron confinement at the nano scale, so-called quantum confinement effects. Quantum confinement occurs when the size of nanoparticles approaches the exciton Bohr radius. The UV–vis findings thus suggest that the Cr-doped ZnS nanoparticles have a promising future for use in opto-electronic devices.

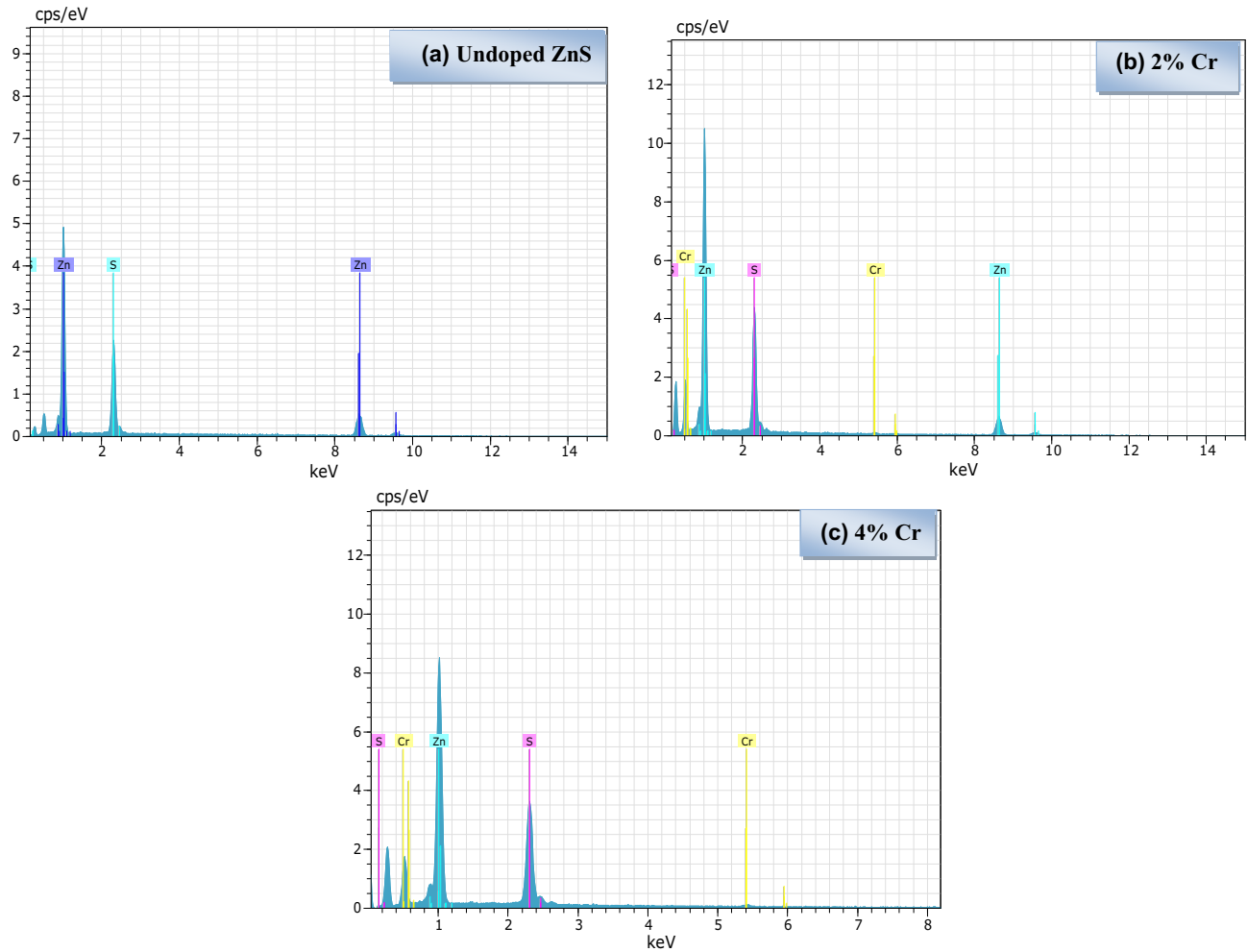


Fig. 4 EDS spectra of Zn_{1-x}Cr_xS nanoparticles

Table 2 Chemical composition of Cr-doped ZnS nanoparticles

Elements	Atomic%		
	0%	2%	4%
Zn	69.24	58.28	59.04
S	30.76	40.90	39.81
Cr	00.00	0.82	1.15
Total	100	100	100

3.5 Dielectric studies

3.5.1 Dielectric constant

Semiconducting nanoparticles with a larger band gap have the potential to be used as a dielectric in capacitors. The amount and type of dopant can greatly influence the optical and dielectric properties

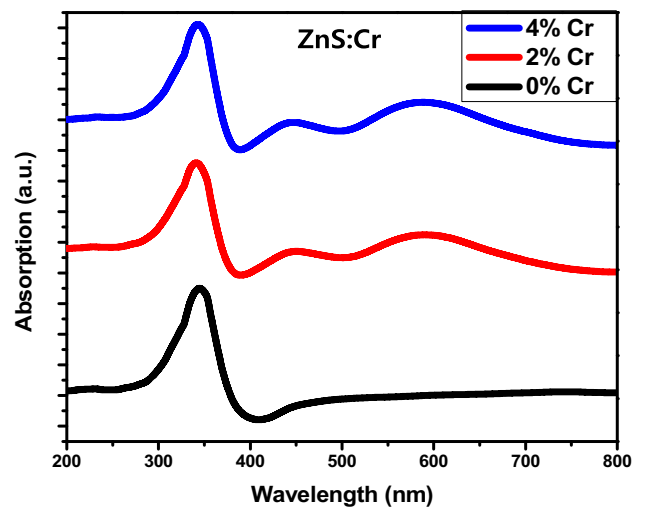


Fig. 5 Absorption spectra of Zn_{1-x}Cr_xS nanoparticles

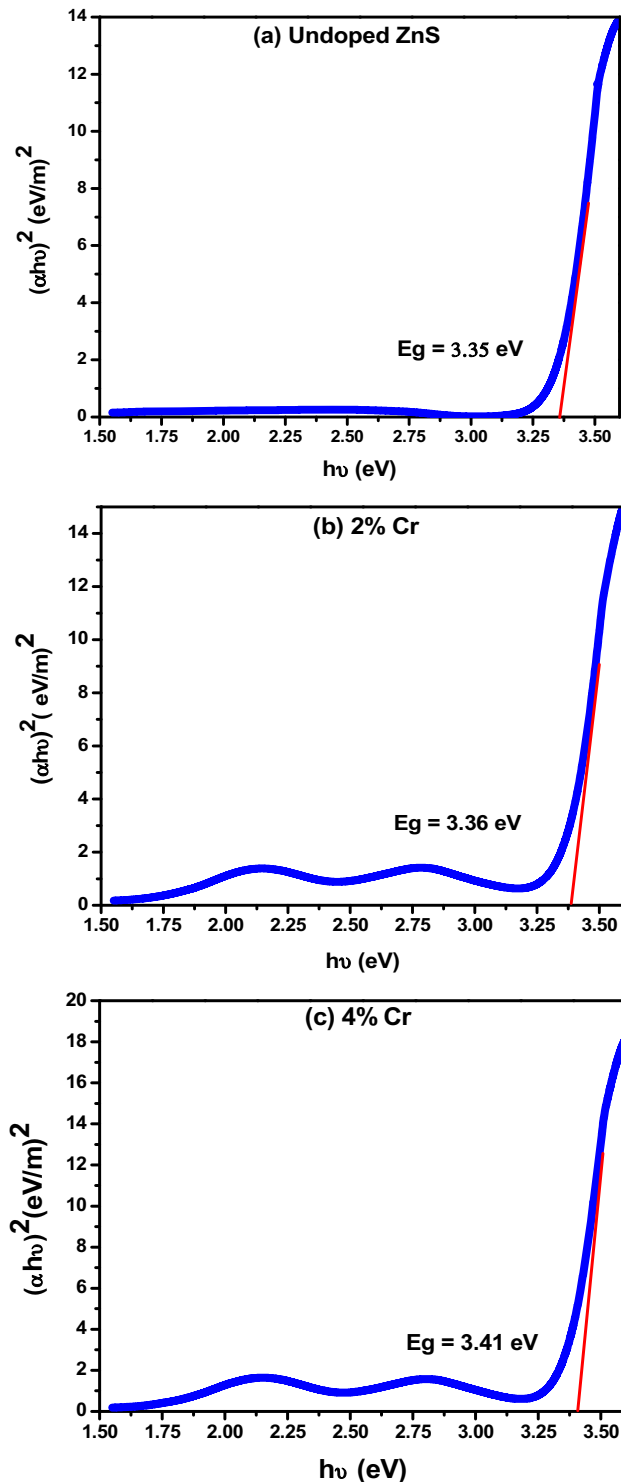


Fig. 6 Tauc's plot of $Zn_{1-x}Cr_xS$ nanoparticles

of nanoparticles. In this study, we measured the dielectric response of undoped and Cr-doped ZnS nanoparticles. The dielectric constant is represented as [45]

$$\varepsilon = \varepsilon' - j\varepsilon'' \quad (6)$$

The first term in the above equation represents the real part of the dielectric constant and describes stored energy, whereas the second term represents the imaginary part of the dielectric constant and describes dissipated energy. The dielectric constant of $Zn_{1-x}Cr_xS$ nanoparticles was measured with an LCR meter at 300 K in the frequency range of 50 Hz to 5 MHz and determined using the equation [45]

$$\varepsilon' = \frac{C_p t}{\varepsilon_0 A}, \quad (7)$$

where C_p is the capacitance of the specimen in Farads, t is the thickness of the pellet, ε_0 is the permittivity of free space ($\varepsilon_0 = 8.8542 \times 10^{-12}$ F/m), and A is the cross-sectional area of the flat surface of the pallet. Figure 7 shows a plot of the dielectric constant versus the logarithm of frequency for all concentrations of chromium, with each sample exhibiting an exponential trend. For all concentrations, the dielectric constant decreases with increasing frequency and becomes nearly constant at high frequencies [45]. The observed dielectric behavior can be explained using the Maxwell-Wagner model [46, 47]. A dielectric medium, according to this model, is made up of two layers of well-conducting grains separated by conducting or resistive grain boundaries. The charge carriers can easily transfer the grains after the application of an external electric field, but they tend to clump together at the grain boundaries. This process can cause significant polarization and hence a high

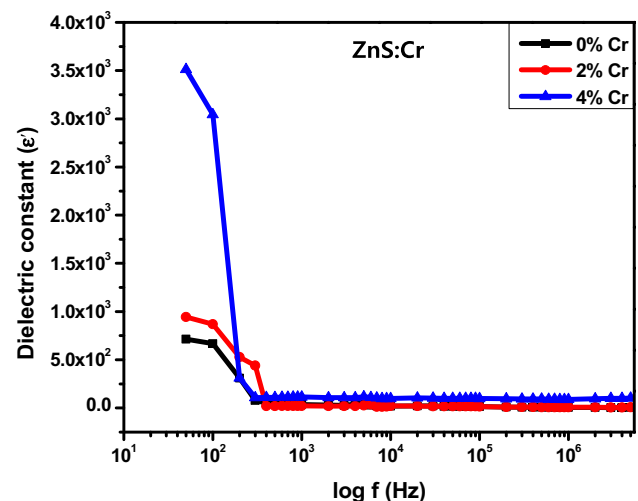


Fig. 7 Variation of dielectric constant with frequency for $Zn_{1-x}Cr_xS$ nanoparticles

dielectric constant at lower frequencies. Beyond a certain frequency of external field, the polarization decreases with increasing frequency and then attains a constant value. In this case, the Cr-doped ZnS nanoparticles have a higher dielectric constant, which decreases as chromium concentration increases. This is due to the presence of chromium at the grain boundaries. Wu et al. [48] discovered a significant increase in the dielectric constant and a corresponding decrease with increasing dopant concentration while investigating Li and Ti-doped NiO-based ceramics. Due to the high value of dielectric constant, the prepared samples are used in capacitors.

3.5.2 Dielectric loss

Figure 8 depicts the variation of dielectric loss as a function of the logarithm of frequency for Zn_{1-x}Cr_xS nanoparticles at room temperature. The dielectric loss is calculated using the equation [45]

$$\epsilon'' = \epsilon' \tan \delta \tag{8}$$

All samples show a frequency-dependent exponential decay of dielectric loss. The dielectric loss for each sample is found to be very high at low frequencies, decreases significantly with increasing frequency, and reaches a constant value at high frequencies. The concentration of Cr dopant also affects dielectric loss. It is obvious that as the concentration of the dopant increases, the dielectric loss decreases.

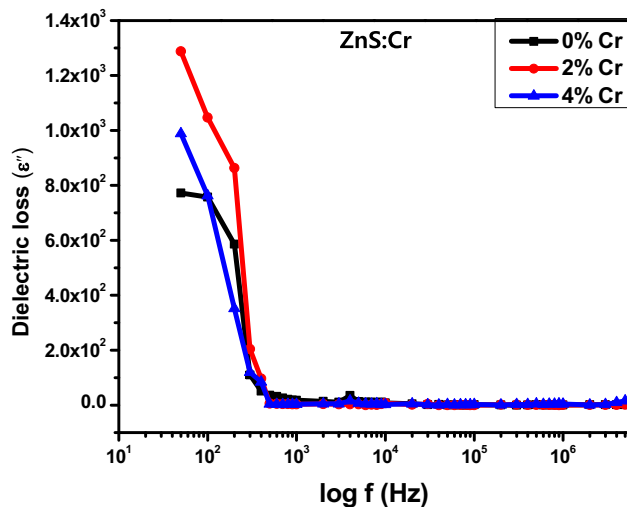


Fig. 8 Variation of dielectric loss with frequency for Zn_{1-x}Cr_xS nanoparticles

quite low, with an observed value of 7.72×10^2 . It increases for 2% Cr and then decreases as the Cr content increases. Virpal et al. [49] also noticed similar behavior while investigating Pb-doped ZnS nanoparticles. The Maxwell–Wagner effect is important in determining the dielectric properties of doped samples. In doped ZnS nanoparticles, the Maxwell–Wagner process causes higher dielectric losses on the lower frequency side. The low dielectric loss values at higher frequencies suggest that the prepared materials can be used in high-frequency device applications.

3.5.3 AC conductivity

The AC electrical conductivity (σ_{AC}) of the Zn_{1-x}Cr_xS nanoparticles can be calculated using the dielectric constant and tangent loss using the equation [50]

$$\sigma_{AC} = 2\pi f \epsilon' \epsilon_0 \tan \delta, \tag{9}$$

where f is the frequency of the applied field. Figure 9 shows the variation of AC electrical conductivity (σ_{AC}) as a function of frequency for Zn_{1-x}Cr_xS nanoparticles at room temperature. The AC conductivity of all samples increases in an exponential manner with increasing frequency. In the low-frequency region, conductivity is almost frequency-independent, whereas it is highly frequency-dependent in the high-frequency region. This behavior could be attributed to the semiconducting nature of nanoparticles [50]. It is obvious that AC conductivity gradually increases with the increasing frequency of the

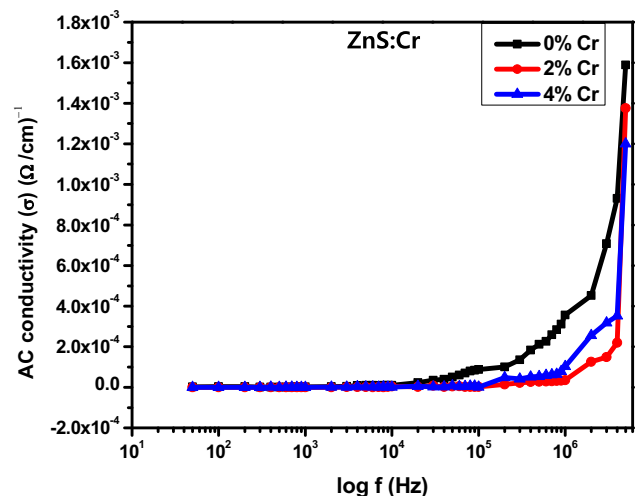


Fig. 9 Variation of AC conductivity with frequency for Zn_{1-x}Cr_xS nanoparticles

applied ac field because increasing frequency enhances electron migration, which is the normal behavior of doped ZnS nanoparticles [51]. Figure 9 also shows that conductivity is greatest for undoped ZnS and decreases with the addition of Cr ions to the ZnS matrix. This could be because the dopant introduces defect ions into the ZnS system, which facilitates the formation of a grain boundary defect barrier, resulting in a blockage of charge carrier flow. As a result, doping reduces AC conductivity.

4 Conclusions

We successfully prepared $Zn_{1-x}Cr_xS$ with $x = 0.00$, 0.02 , and 0.04 nanoparticles of crystallite size 1.70 – 1.56 nm using the co-precipitation method. All samples exhibited a single-phase cubic structure. FE-SEM images of Cr-doped ZnS nanoparticles revealed a decrease in the agglomeration of particles with an increase in Cr content. The incorporation of Cr into doped samples was verified by EDS analysis. Doping ZnS nanoparticles with chromium increased the band gap energy from 3.35 eV to 3.41 eV, which could be attributed to a decrease in crystallite size. Furthermore, the doped nanoparticles have a higher dielectric constant, which decreases as chromium concentration increases. This is due to the presence of chromium at the grain boundaries. All samples have low dielectric loss at higher frequencies, whereas AC conductivity increases abruptly at higher frequencies but decreases with increasing Cr content.

Author contributions

Material preparation, data collection, and analysis were performed by VVJ. The first draft of the manuscript was written by VVJ. BSM commented on previous versions of the manuscript. Authors read and approved the final manuscript.

Funding

I have declared that no funds, grants, or other support were received during the preparation of this manuscript.

Data availability

The datasets generated during and/or analyzed during the current study are available from the corresponding author on reasonable request.

Declarations

Conflict of interest The authors declare that they have no known competing financial interests or personal relationships that could have appeared to influence the work reported in this paper.

Ethical approval Disclosure of potential conflicts of interest.

References

1. P. Caregnato, K.R. Espinosa Jiménez, P.I. Villabrille, *Catal Today* **372**, 183–190 (2020)
2. A. Phuruangrat, S. Siri, P. Wadbuwa et al., *J. Phys. Chem. Solids* **126**, 170–177 (2019)
3. K. Ou, S. Wang, G. Wan, M. Huang, Y. Zhang, L. Bai, L. Yi, *J. Alloys Compd.* **726**, 707–711 (2017)
4. H. Hu, W. Zhang, *Opt. Mater.* **28**, 536–550 (2006)
5. S. Ghorai, N. Patra, A. Pal, D. Bhattacharyya, S.N. Jha, B. Ray, S. Chatterjee, A.K. Ghosh, *J. Alloys Compd.* **805**, 363–378 (2019)
6. S.J. Pearton, D.P. Norton, K. Ip, Y.W. Heo, T. Steiner, *J. Vac. Sci. Technol. B* **22**, 932–948 (2004)
7. N. Kumbhojkar, V.V. Nikesh, A. Kshirsagar, S. Mahamuni, *J. Appl. Phys.* **88**, 6260–6264 (2000)
8. A. Reddy, G. Murali, R.P. Vijayalakshmi, B.K. Reddy, *Appl. Phys. A* **105**, 119–124 (2011)
9. N.V. Desai, I.A. Shaikh, K.G. Rawal, D.V. Shah, *AIP Conf. Proc.* **1953**, 030149 (2018)
10. Z. Zhang, J. Li, J. Jian, R. Wu, Y. Sun, S. Wang, Y. Ren, J. Li, *J. Cryst. Growth* **372**, 39–42 (2013)
11. A. Azmand, H. Kafashan, *J. Alloys Compd.* **779**, 301–313 (2019)
12. S.J. Basha, V. Khidhirbrahmendra, J. Madhavi, U.S.U. Thampy, C.V. Reddy, R.V.S.S.N. Ravikumar, *Adv. Mater. Devices* **4**, 260–266 (2019)
13. J. Ghrayeb, T.W. Jackson, R. Daniels, D.G. Hopper, *Proc. SPIE* **3057**, 237 (1997)
14. O.A. Korotchenkov, A. Cantarero, A.P. Shpak, Y.A. Kunitskii, A.I. Senkevich, M.O. Borovoy, A.B. Nadtochii, *Nanotechnology* **16**, 2033 (2005)

15. A.Z. Obidin, A.N. Pechenov, Y.M. Popov, V.A. Frolov, Y.V. Korostelin, P.V. Shapkin, *Sov. J. Quantum Electron.* **18**, 1100 (1988)
16. X. Fang, T. Zhai, U.K. Gautam, L. Li, L. Wu, Y. Bando, D. Golberg, *Prog. Mater. Sci.* **56**, 175–287 (2011)
17. Y. Jiang, W.J. Zhang, J.S. Jie, X.M. Meng, J.A. Zapien, S.T. Lee, *Adv. Mater.* **18**, 1527–1532 (2006)
18. M. Narayanan, S. Kumarasamy, M. Ranganathan, S. Kandasamy, G. Kandasamy, K. Gnanavel, K. Mamtha, *Mater. Today* (2020). <https://doi.org/10.1016/j.matpr.2020.05.725>
19. L.J. Zhuge, X.M. Wu, Z.F. Wu, X.M. Chen, Y.D. Meng, *Scr. Mater.* **60**, 214 (2009)
20. L. Schneider, S.V. Zaitsev, W. Jin, A. Kompch, M. Winterer, M. Acet, G. Bacher, *Nanotechnology* **20**, 135604 (2009)
21. A. Iqbal, A. Mahmood, T.M. Khan, E. Ahmed, *Progr. Nat. Sci.* **23**(1), 64–69 (2013)
22. N.A. Vlasenko, P.F. Oleksenko, M.A. Mukhlyo, Z.L. Denisova, L.I. Veligura, *Ann. Phys.* **525**(12), 889–905 (2013)
23. M. Nematollahi, X. Yang, U.J. Gibson, T.W. Reenaas, *Thin Solid Films* **590**, 28–32 (2015)
24. A. AL-Osta, A. Alnehia, A.A. Qaid, H.T. Al-hsab, A. Al-Sharabi, *Optik* **214**, 164831 (2020)
25. C.M.S. Vall, M. Chaik, A. Tchenka, S. Hnawi, A. Mellalou, A.E. Kissani, M. Aggour, A. Outzourhit, *Physica E* **130**, 114694 (2021)
26. D.A. Reddy, A. Divya, G. Murali, R.P. Vijayalakshmi, B.K. Reddy, *Physica B* **406**, 1944–1949 (2011)
27. P.S. Prabhu, P. Kathirvel, H.B. Ramalingam, *Mater. Today* **5**, 16466–16471 (2018)
28. M. Aqeel, M. Ikram, A. Asghar, A. Haider, A. Ul-Hamid, M. Naz, M. Imran, S. Ali, *Appl. Nanosci.* **10**, 2045–2055 (2020)
29. V.J. Kumar, R. Thangaraj, S. Sharma, R.C. Singh, *Appl. Surf. Sci.* **416**, 296–301 (2017)
30. O. Gurbuz, M. Okutan, *Appl. Surf. Sci.* **387**, 1211–1218 (2016)
31. A. Selmi, A. Fkiri, J. Bouslimi et al., *J. Mater. Sci.* **31**, 18664–18672 (2020)
32. R. Khan, C.I.L. de Araujo, T. Khan, S.A. Khattak, E. Ahmed, A. Khan et al., *J. Mater. Sci.* **30**, 3396–3404 (2019)
33. G.N. Mathur, *Prog. Cryst. Growth Charact. Mater.* **45**, 167–169 (2002)
34. S.K. Mandal, S. Chaudhuri, A.K. Pal, *Thin Solid Films* **209**, 230 (1999)
35. R. Thielsch, T. Böhme, H. Böttcher, *Phys. Status Solidi A* **155**, 157–170 (1996)
36. T. Ming, C. Weiping, Z. Lide, *Appl. Phys. Lett.* **71**, 3697 (1997)
37. S. Elsi, S. Mohanapriya, K. Pushpanathan, *J. Supercond. Novel Magn.* **33**, 3223–3240 (2020)
38. K. Bera, S. Saha, P.S. Jana, *Mater. Today* **5**, 6321–6328 (2018)
39. B. Poornaprakash, K.N. Kumar, U. Chalapathi, M. Reddeppa, P.T. Poojitha, S.-H. Park, *J. Mater. Sci.* **27**(6), 6474–6479 (2016)
40. P. Kaur, S. Kumar, A. Singh, C.L. Chain, C.L. Dong, T.S. Chan, K.P. Lee, C. Srivastava, S.M. Rao, M.K. Wu, *Superlattices Microstruct.* **84**, 785–795 (2015)
41. K. Ichino, Y. Morimoto, H. Kobayashi, *Phys. Stat. Sol.* **779**(4), 776–779 (2006)
42. D. Anbuselvan, S. Muthukumaran, *Opt. Mater.* **42**, 124–131 (2015)
43. C. Mrabet, O. Amount, A. Boukhachem, M. Amlouk, T. Manoubi, *J. Alloys Compd.* **648**, 826–837 (2015)
44. J.X. Wang, X.W. Sun, Y. Yang, H. Huang, Y.C. Lee, O.K. Tan, L. Vayssieres, *Nanotechnology* **17**, 4995 (2006)
45. S.A. Ansari, A. Nisar, B. Fatma, W. Khan, A. Naqvi, *Mater. Sci. Eng. B* **177**, 428–435 (2012)
46. J. Maxwell, *Oxford Univ. Press* **1**, 328 (1873)
47. K.W. Wanger, *Ann. Phys. (Leipzig)* **40**, 817 (1913)
48. C.-W. Wu, Y. Nan, Y. Lin, Y. Deng, *Phys. Rev. Lett.* **89**, 217601 (2002)
49. A.H. Virpal, S. Sharma, R.C. Singh, *Appl. Surf. Sci.* **372**, 57–62 (2016)
50. S. Suresh, C. Arunseshan, *Appl. Nanosci.* **4**(2), 179–184 (2014)
51. R. Zamiri, A. Kaushal, A. Rebelo, J.M.F. Ferreira, *Ceram. Int.* **40**(1), 1635–1639 (2014)

Publisher's Note Springer Nature remains neutral with regard to jurisdictional claims in published maps and institutional affiliations.

Springer Nature or its licensor holds exclusive rights to this article under a publishing agreement with the author(s) or other rightsholder(s); author self-archiving of the accepted manuscript version of this article is solely governed by the terms of such publishing agreement and applicable law.